Encapsulation of β-alanine model amino-acid in zirconium(IV) metal organic frameworks: defect engineering to improve host guest interactions.

Asier R. Muguruza[1,2], Roberto Fernandez de Luis[2], Naroa Iglesias[2], Begoña Bazán[2,3], Miren-Karmele Urtiaga[3], Edurne S. Larrea[3], Arkaitz Fidalgo-Marijuan[2], Gotzone Barandika[1,2*]

[1] Dept. of Inorganic Chemistry, Universidad del País Vasco (UPV/EHU), Barrio Sarriena s/n, Leioa, Bizkaia, 48940, Spain

[2] BCMaterials, Ed. Martiana Casiano, Barrio Sarriena s/n, Leioa, Bizkaia, 48940, Spain

[3] Dept. of Mineralogy and Petrology, Universidad del País Vasco (UPV/EHU), Barrio Sarriena s/n, Leioa, Bizkaia, 48940, Spain

*Corresponding author: gotzone.barandika@ehu.eus

Juan Manuel Salas Peregrín, *in memoriam*

Keywords: drug delivery systems; encapsulation; zirconium(IV)-based metal organic frameworks; defect engineering; β-alanine; host-guest interactions

Abstract

Metal-Organic Frameworks (MOFs) are porous coordination networks assembled through metal complexes with organic linkers. Due to their chemical versatility, these materials are being investigated for various applications including gas storage and separation, biomedicine and catalysis. The aim of this work is the encapsulation of the model β-alanine amino-acid in the nanostructured zirconium-based MOF (UiO-66) which contains the ligand H_2BDC (1,4-benzenedicaboxylic acid). Additionally, ligand functionalization (by using H_2doBDC (2,5-dihydroxy-1,4-benzenedicarboxylic acid) and defect engineering have been

carried out to produce UiO-66 derivatives, in order to modify the host-guest interactions, and hence study their influence on the β-alanine loading capacity and release kinetics. The as-obtained materials have been characterized by X-ray diffraction (XRD), X-ray thermo diffraction (TDX), infrared (IR) spectroscopy, thermogravimetric analysis-differential scanning calorimetry (TG-DSC) and elemental analysis (EA). Morphology of nanoscale MOFs has been explored by transition electron microscopy (TEM). Adsorption isotherms have been constructed, and the concentration of β-alanine in the post-adsorption solution (supernatant) has been quantified by high performance liquid chromatography coupled with mass spectroscopy (HPLC-MS) and EA. Adsorption capacity values indicate that the presence of hydroxyl groups at the organic linker H_2doBDC enhances the host-guess affinity between the framework and the adsorbate β-alanine. The influence of defect engineering, on the adsorption however, is not that obvious. On the other hand, desorption experiments show similar behaviour for H_2doBDC-based derivatives. An adsortion mechanism has been proposed consisting of a combination of host-guest interaction at low concentrations, and covalent anchoring/ligand displacement by β-alanine at the inorganic clusters.

1. INTRODUCTION

Metal-Organic Frameworks (MOFs) consist of metal or cluster nodes linked by organic molecules (ligands) which crystallize of pores and cavities with adjustable size, shape and chemistry [1]. Depending on the connectivity of the inorganic and organic units, some of these coordination compounds exhibit a combination of high surface area, small pore windows and specific pore´s surface chemistry, which enables them to perform as host structures for specific guest molecules [2]. In consequence, MOFs can be used as bio-active low molecular weight molecules reservoirs, paving the way to the design of controllable Drug Delivery Systems (DDSs) [3].

Encapsulation and controlled release of organic molecules from MOF carriers not only depend on the surface area or pore window apertures, but also on the affinity between host and guest species, which is mainly controlled by parameters such as electrostatic forces, the nature of the metal nodes, hydrogen bonds, and π-π, acid-base and hydrophobic interactions [4-9].

Taking into account all of the characteristics previously mentioned for the design of MOF-based drug delivery systems (DDSs) [10-12], MOF with 1) high chemical stability, 2) tuneable porosity, 3) capacity for pre and post functionalization, and 4) demonstrated bio-compatibility are required. These are characteristics attached to zirconium terephthalate MOF materials (also known as UiO-66, where UiO stands for Universitet i Oslo) and this is the reason why it has been selected for this work.

UiO-66 has an ideal formula of $[Zr_6O_4(OH)_4(BDC)_6]$; in which H_2BDC is 1,4-benzenedicarboxylic acid or terephthalic acid (Figure 1), and its structure is assembled from zirconium(IV) hexanuclear clusters inorganic building units widely present in zirconium MOFs (Figure 2 (a.1.) and (b.1)) [13].

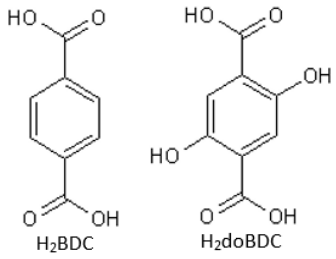

Figure 1. Organic linkers H_2BDC (1,4-benzenedicaboxylic acid) and H_2doBDC (2,5-dihydroxy-1,4-benzenedicarboxylic acid)

The inorganic node consists of an inner $Zr_6O_4(OH)_4$ cluster in which the triangular faces of the Zr_6-octaedra are alternatively capped by μ_3-O and μ_3-OH groups. All of the polyhedron

edges are bridged ideally by twelve carboxylate groups (Figure 2 (a.2)). Each BDC ligand is shared by two of them giving rise to a face-centred cubic net showing an fcu 12-connected topology (Figure 2 (a.1)).

The ortho position of hydroxyl and carboxyl groups in H2doBDC also occurs in the lighter molecule salicylic acid (IUPAC name is 2-hydroxybenzoic acid). When coordinated to metal ions, salicylate binding modes occur frequently, like in the iron transport systems in microbes and the coordination chemistry of siderophores. Most notable siderophores include enterobactin, desferrioxamine B, alcaligin and bacillibactin, and significant studies on the matter have been carried out by Prof. K. N. Raymond and co-workers during decades [14, 15].

The combination of a highly connected nodes and chemical stable Zr-O-C-benzene moieties within the framework confers to UiO-66 materials and its derivatives the initially required chemical stability. Regarding the porosity of ideal UiO-66 structure, there are four octahedral and eight tetrahedral pores per unit cell. On the other hand, the BET specific surface area of materials has been calculated (BET stands for Brunauer-Emmett-Teller theory) leading to a value of 1067 cm^2g^{-1}, while porous volume is 680 $Å^3$ per formula unit. Furthermore, thanks to the chemical versatility of UiO-66, different isoreticular frameworks can be obtained by pre-synthetic functionalization of H_2BDC ligand or applying post-synthetic modification strategies.

The chemical lability of Zr-based frameworks goes beyond the defect engineering during the synthesis, since these defective positions have been used as post-synthesis anchoring points for carboxyl bearing molecules [16]. Even more, post-synthetic ligand displacements within the MOF frameworks is also possible when immersing the material in a high concentrated solutions of specific molecules containing bridging motifs that can displace the Zr-Carboxylate bonds [17]. The above describes chemical malleability of MOF materials

offer an additional drug adsorption mechanisms on MOFs, apart from the organic molecules adsorption based on host-guest interactions.

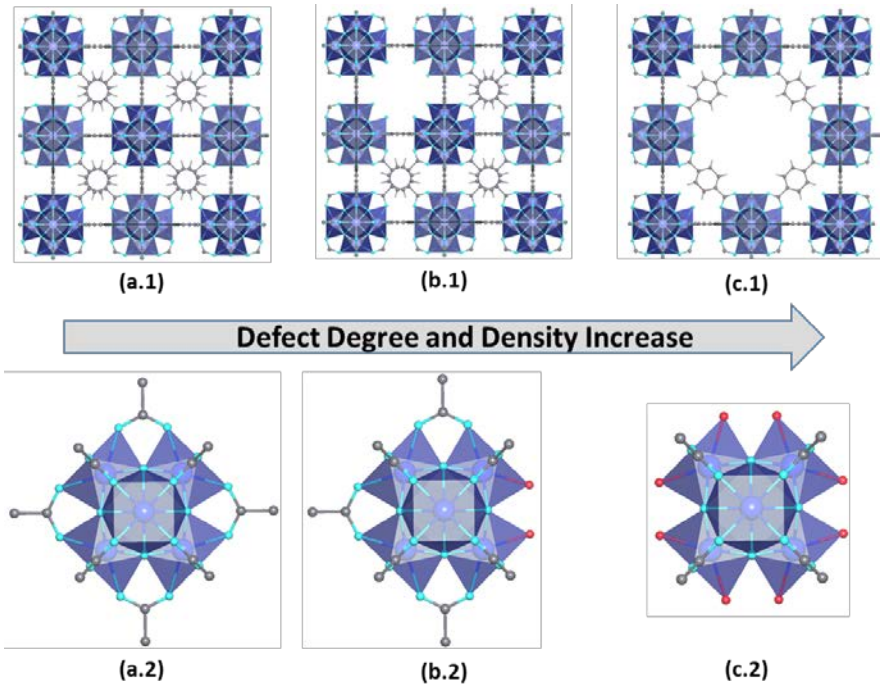

Figure 2. (a.1) and (a.2) Ideal UiO-66 crystal structure and 12-c zirconium hexameric clusters. Detail of (b.1) Ligand defect and (c.1) cluster defects within the UiO-66 framework. (b.2) Representation of possible local structures for nearly ideal 11/12 connected non defective and (c.2) 8/12 defective zirconium clusters. Zirconium atoms are coloured in dark blue, oxygen in light blue and carbon in grey. Red spheres indicate coordinated species for charge neutrality and saturation of coordination environment.

Experimentally, synthesis conditions such as temperature, solvents and inorganic or organic modulators, among others, influence drastically the particle size, morphology, surface area and porosity, as well as the local structure of UiO-66 and derivative materials. Indeed, particle size and morphology of UiO-66 and iso-reticular derivatives have been modulated

between 20 nm and micron scale. Diverse crystal morphologies have been also obtained, from spheres, truncated cubes or cuboctahedron. Internal surface area and external particle size and morphology have a great impact on the surface chemistry and chemical stability of zirconium terephthalate based materials; being also relevant characteristics for the bio-active molecules uptake and release processes in DDSs systems. Besides the easy modifiable porosity or particle size, one of the most fascinating characteristics of zirconium terephthalate is their defect crystal chemistry. The use of co-crystallization organic (formic acid, acetic acid, benzoic acid) and inorganic agents (HCl, HNO_3, H_2SO_4) during the crystallization can generate linker (Figure 2 (b.1)) and cluster (Figure 2 (b.2)) point defects within the framework. Defect engineering also induces surface area to increase from values close to 1000 $m^2 \cdot g^{-1}$, reported for nearly non-defective compound (11/12 connectivity of the clusters), to values close to 1450 $m^2 \cdot g^{-1}$ in the higher defect density UiO-66 frameworks (8/12 connectivity). Porous structure is also altered with defect inclusion within UiO-66. Defective samples usually exhibit pores with higher diameters, and more spread pore size distribution than nearly non-defective samples. Depending on the nature of the modulator, local structure and chemistry of zirconium clusters at defective positions is also altered [18-20]. Terephthalate linkers of UiO-66 frameworks are partially replaced at defective positions when mono-carboxylate acids are used within the synthesis media [21]. When inorganic acids are applied as defect engineering tool, the organic linker is replaced by an hydroxyl and a water molecule per defective position [22, 23]. Regardless the synthesis conditions, it is foreseen certain degree of defects density within the UiO-66 materials, being 8/12 the minimum coordination number for zirconium clusters induced by defect generation (Figure 2 (c.2)) [24, 25].

Finally, even achieving the best performance for a DDSs in terms of uptake and release capacity and kinetics, the biocompatibility of UiO-66 and its derivatives is also a crucial

factor. Indeed, non-functionalized UiO-66, with particle size within the micron scale (produced by solvo-thermal synthesis in DMF), was determined non-toxic due to its biologically inert metal cluster and organic ligand [26].

The chemical and structural versatility of UiO-66 materials, added to its biocompatibility, has triggered their use in a wide range of DDSs applications. In fact, DDSs based on UiO-66 have been designed for multiple bioactive molecules, such as alendronate (osteoporosis treatment) [27], fluorouracil (cancer treatment) [28], chloramphenicol and ibuprofen (antibiotic and anti-inflammatory) [29], and zidovudine (antiretroviral) [30], among others. Despite the wide range of studies tackling the encapsulation or adsorption of bio-active guest species on MOF materials, none of these previously published works has been focused on one of the most important group of biologically relevant molecules: the amino acids.

With the goal of designing a DSSs, this works has been focused on the synthesis of UiO-66 and its di-hydroxyl derivative compound UiO-66-$(OH)_2$, which is iso-reticular with the original UiO-66 [29, 31]. Taking into account the chemical structure of amino acids, we have considered that the incorporation of di-hydroxyl motifs within the UiO-66-$(OH)_2$ framework, will act as hydrogen bonding points for amino-acids encapsulation. In addition, porous structure of UiO-66 and UiO-66-$(OH)_2$ materials have been modified including different defect degrees within the frameworks; which is foreseen to modify the amino acid molecules uptake capacity and release kinetics. Furthermore, all the materials have been crystallized in the nano-range size suitable for their incorporation into cells. In summary, the following four samples: UiO-66$|_{10/12}$, UiO-66$|_{8,2/12}$ and UiO-66-$(OH)_2|_{11/12}$ and UiO-66-$(OH)_2|_{8,2/12}$ have been fully characterized and studied over β-alanine adsorption. These samples go from original to functionalized material (from UiO-66$|_{10/12}$ to UiO-66-$(OH)_2|_{11/12}$)

and from non defective to defective material (from UiO-66|$_{10/12}$ to UiO-66|$_{8,2/12}$ and from UiO-66-$(OH)_2$|$_{11/12}$ to UiO-66-$(OH)_2$|$_{8,2/12}$).

varying the functionalization motifs at the organic linkers (*i.e. without and with hydroxyl groups*) and the defect degree of the compound

From the adsorbate point of view, β-alanine (IUPAC name is 3-aminopropanoic acid) has been selected as a model amino acid to be encapsulated within UiO-66 and its derivative di-hydroxyl UiO-66-$(OH)_2$ (figure 3) The selection of β-alanine as adsorbate in this work is explained because of its low molecular weight ($C_3H_7NO_2$, 89.09318 g·mol^{-1}). In addition, its carboxylic and amine groups are thought to be appropriate for interaction with UiO-66 and its derivatives. It is worth mentioning that β-alanine has been also used in sports to improve the performance of high-intensity exercises [32] because it is the rate-limiting precursor of the dipeptide carnosine. Recent studies confirm that carnosine and anserine homeostasis in skeletal muscle and heart is controlled by β-alanine transamination [33].This is the reason why the stability of β-alanine has been studied to conclude that most of the β-alanine is degraded and used as an energy source [34]. In fact, in 1955 Pihl and Fritzson reported that more than 90% of the injected C14-labeled β-alanine in rats was recovered in the expired CO_2, suggesting that β-alanine was used as a carbon source for energy provision through oxidation [35]. As a result of this, β-alanine supplementation has been concluded to be a rather impractical process for sport objectives [36].

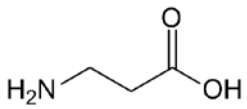

Figure 3. Structure of β-alanine.

In summary, this work explores the relationship between both the generation of defects and the presence of hydroxyl groups with the β-alanine loading capacity of and release kinetics of UiO-66-based-nanoparticles.

2. EXPERIMENTAL

The following nomenclature has been used for the materials: UiO-66$|_{X/12}$ and UiO-66-$(OH)_2|_{X/12}$ where UiO-66 is $[Zr_6O_4(OH)_4(BDC)_6]$, UiO-66-$(OH)_2$ is $[Zr_6O_4(OH)_4(doBDC)_6]$ and X is the number of carboxyl groups anchored per inorganic cluster (X=12 for the ideal cluster (Figure (a.2)). As it has been schematically depicted in the Figures 1 (a.2), (b.2) and (c.2) the inner structure of the cluster, as well as this for UiO-66 materials (Figure (a.1), (b.1) and (c.1)) remains the same independently on the linker defect degree. In this UiO-66 and UiO-66-$(OH)_2$ defective compounds have been generated through the incorporation of HCl in the synthesis media. The average number of linkers, and hence the linkers defect density within the compounds, have been described by the X values in the compounds short-names, e.g. UiO-66$|_{X/12}$ and UiO-66-$(OH)_2|_{X/12}$. All reagents were purchased from Sigma-Aldrich, and used without further purification.

Synthesis of raw materials: Four materials were prepared: UiO-66$|_{10/12}$, UiO-66$|_{8,2/12}$ and UiO-66-$(OH)_2|_{11/12}$ and UiO-66-$(OH)_2|_{8,2/12.}$ Synthesis of UiO-66$|_{10/12}$ was carried out by mixing $ZrCl_4$ and H_2BDC in DMF and water. The mixture was stirred at room temperature until a white dispersion was obtained. Then, the suspension was transferred into a close vessel and it was incubated for 24 h at 80 ^oC. After letting the vessel cooling down a white gel of UiO-66$|_{10/12}$ was obtained. The synthesised compound was washed with DMF (2 x 10 mL) and MeOH (2 x 10 mL) and dried at 80 ^oC for 24 h, achieving a dried monolith. To obtain UiO-66$|_{8,2/12}$, 1mL of concentrated HCl was added to the $ZrCl_4$ and H_2BDC mixture. The rest

of the procedure is similar to the one used to obtain UiO-66|$_{10/12.}$ In order to prepare UiO-66-(OH)$_2$|$_{11/12}$, the procedure is similar to that previously described for UiO-66|10/12 but using H2doBDC as an organic linker, yielding a yellow gel. Similarly, to obtain UiO-66-(OH)$_2$|$_{8,2/12}$ 1mL concentrated HCl was added to the reaction media after mixing $ZrCl_4$ and H_2doBDC. Additional details of synthesis conditions are available in the supplementary material (Table S1).

Activation of raw materials: Activation of the samples consists of the elimination of solvent molecules to produce empty pores to favour the encapsulation of β-alanine. With this aim, a second heating process was performed under vacuum. Solid samples were grinded and dried under vacuum at 120 ^{o}C (for UiO-66|$_{x/12}$ samples) or at 100 ^{o}C (for UiO-66-(OH)$_2$|$_{x/12}$ samples) for 24 h. Activation temperatures were chosen based on XRD, TG and TDX analyses (Results and Discussion Section). Activation temperature in vacuum was set at 120 ^{o}C for UiO-66|$_{10/12}$ and UiO-66|$_{8,2/12}$ samples and at 100 ^{o}C for UiO-66-(OH)$_2$|$_{11/12}$ and UiO-66-(OH)$_2$|$_{8,2/12}$.

β-alanine adsorption and desorption batch experiments: For the assays of β-alanine adsorption, samples of UiO-66|$_{10/12}$, UiO-66|$_{8,2/12}$, UiO-66-(OH)$_2$|$_{11/12}$ and UiO-66-(OH)$_2$|$_{8,2/12.}$ (≈ 40 mg) were dispersed in 5 mL of different β-alanine aqueous solutions (pH= 7.11). The samples were stirred over 5 days at room temperature and at 1000 rmp. Afterwards, the loaded samples were centrifuged and the supernatant recovered by filtration. Samples were dried at 80^{o}C for 2 days and β-alanine aqueous supernatants were kept frozen until HPLC/MS analyses were performed, to prevent β-alanine degradation. For high concentration points, triplicate analyses were carried out to quantify the maximum error expected within the obtained adsorption isotherms. β-alanine desorption tests were carried out on 100 mg of UiO-66-(OH)$_2$|$_{11/12}$ and UiO-66-(OH)$_2$|$_{8,2/12}$. materials previously charged in 5000 ppm solution. Desorption processes were performed in 100 mL of aqueous

solutions at neutral (pH=7) and slightly acidic media (pH=4). pH value was adjusted with HCl and NaOH 0.1M and 0.01M solutions.

Structural and thermal characterization: X-ray diffraction was performed on polycrystalline samples. All diffractograms were obtained by a Philips PW1710, with a Bragg-Brentano geometry copper anticathode and a primary monochromator (CuK_α). The measurements were executed between 5 and 70˚ in 2θ, with a step of 0.02˚. X-ray thermo diffraction (TDX) measurements were performed with a Bruker D8 Advance Vantec diffractometer for polycrystalline samples (theta-theta geometry with temperature chambers, CuK_α, solid stated detector SolX with a discrimination window). Measurements were performed from 30˚C to 400˚C. Patterns were acquired each 15˚C. Infrared spectra were registered in a range wavenumber between 4000 and 400 cm^{-1} by means of a spectrophotometer with Fourier transformation JASCO FT/IR-6100. Thermogravimetric analysis and differential scanning calorimetry (TG-DSC) were performed by using a NETZSCH STA 449 F3 Simultaneous DSC-TGA thermobalance, under a synthetic air atmosphere (60% N_2 + 40% O_2). Heating rate was 5 ˚C/min and data were registered between 30 and 600 ˚C. Non-loaded samples were dried in order to avoid water adsorption during manipulation processes. Elemental analyses were performed by an Euro AE Elemental Analyzer /CHNS). Transmission electron microscopy (TEM) studies were conducted using a Philips Supertwin CM200 transmission microscope operated at 200 kV and equipped with a LaB_6 filament and EDAX-DX-4 microanalysis system.

High performance liquid chromatography coupled with mass spectroscopy (HPLC-MS): Concentration of β-alanine in the post-adsorption solution (supernatant) was determined by means of chromatographic separation in a high performance liquid chromatograph (HPLC, Alliance e2695) coupled to a triple quadrupole mass spectrometer (QqQ, Quattro Micro Micromass) by an electrospray ionization source in positive mode (ESI^+). All the data

were obtained from Waters Cromatografia S.A. The optimization for β-alanine determination was based in the optimization of cones' voltage (CV) and collision energy (CE); in order to establish suitable transitions for the quantification and confirmation (MRM mode). For that a β-alanine aqueous solution of 20 ppm was used and injected multiple times in different conditions. Optimum conditions are shown in table S2. The chromatographic separation was achieved using a Kinetex C18 column (2.6 µm, 2.1 × 50 mm i.d.) with an in-line filter (0.1 mm i.d.) from Phenomenex and a binary A/B gradient (solvent A: water with 0.1 % formic acid and solvent B: acetonitrile with 0.1 % formic acid). The gradient program was established as follows: initial conditions were 1 % B, held at 1 % B for 5 min, raised to 99 % B over 1 min, held at 100 % B until 8 min, decreased to 1 % B over the next 1 min and held at 1 % B until 19 min for re-equilibration of the system prior to the next injection. A flow rate of 0.2 mL/min was used, the column temperature was 30 °C, the autosampler temperature 4 °C and the injection volume 10 µL. Regarding the mass spectrometer conditions, the source temperature was set to 120 °C and the desolvation temperature to 350 °C. The capillary voltage was 3.2 kV and the cone voltage 15 V. Nitrogen was used as the desolvation gas at a flow rate of 600 L/h. Mass data were acquired in the multiple reaction mode (MRM) using two transitions, one for the quantification (90 → 72 u) and the other for the qualification (90 → 30 u). The quantification of β-alanine was performed with an external calibration containing target compound at concentrations ranging from 0.25 to 10 ppm in water. The samples were diluted in water for the analysis (final theoretical concentration around 1-2 ppm).

As studied samples' supernatants were diluted until the final concentration was comprised between 0.25 and 10 ppm of target compound. It is worth mentioning that the higher the concentration of the supernatant, the higher the dilution of the solution to be measurable by HPLC/MS is, and the higher the methodological error included in the analysis. For

example, 3000 times dilution of the most concentrated samples (5300 ppm) has to be carried out the final supernatant solution to be measurable. Due to this process, the obtained results in the high concentration region should be analysed carefully.

3. RESULTS AND DISCUSSION

Synthesis and characterization of the raw materials

Synthesis of UiO-66|$_{10/12}$, UiO-66|$_{8,2/12}$, UiO-66-$(OH)_2$|$_{11/12}$ and UiO-66-$(OH)_2$|$_{8,2/12}$ was carried out as explained above, and X-ray diffraction was performed over the polycrystalline samples in order to confirm the purity of the products. As observed in figure S1, samples UiO-66|$_{8,2/12}$ and UiO-66-$(OH)_2$|$_{8,2/12}$ exhibit higher crystallinity, and this can be attributed to the addition of HCl. Pattern matching analyses [37] were carried out (figure S1), confirming that the four samples are iso-reticular with UiO-66 framework (cubic space group, Fm-3c). Crystal data of UiO-66 [13] were used as starting values for pattern matching. Cell parameters and values for the adjustment are shown in table S3.

X-ray diffraction data produces average structural information of the synthesised compounds, without the possibility to going more in deep in the defects density generated during the crystallization process. Defect density quantification for each phase, and hence the estimation of its chemical formula is not straightforward, and has been approached by using data coming from elemental and thermogravimetric analysis. It is worth mentioning that all the samples have been dried before the measurements to minimize the experimental uncertainties on weigh and chemical percentage changes coming from water adsorption.

Thermogravimetric analyses for all the samples were carried out and the results are shown in figure S2. A similar tendency is observed for all the compounds; in a first step a mass loss is associated to the removal of crystallization water molecules. The second mass loss is

ascribed to the loss of hydroxyl and water species coordinated to the zirconium clusters and solvent molecules interacting more strongly with the structure. Finally, in a third step, the calcination of the BDC and doBDC occurs. The experimental and calculated mass losses, as well as the molecules lost during the processes for all the studied compounds are summarized in table S4. Table 1 summarizes the chemical formula proposed for UiO-66|$_{10/12}$, UiO-66|$_{8,2/12}$, UiO-66-(OH)$_2$|$_{11/12}$ and UiO-66-(OH)$_2$|$_{8,2/12}$

Table 1. Chemical formula for raw materials

Compound	**Chemical formula**
UiO-66|$_{10/12}$	$[Zr_6O_4(OH)_6(H_2O)_2(BDC)_5]\cdot 1.5DMF\cdot 6.5H_2O$
UiO-66|$_{8,2/12}$	$[Zr_6O_4(OH)_{7,8}(H_2O)_{3,8}(BDC)_{4,1}]\cdot 0.75DMF\cdot 5H_2O$
UiO-66-(OH)$_2$|$_{11/12}$	$[Zr_6O_4(OH)_5(H_2O)(doBDC)_{5,5}]\cdot 3.25DMF\cdot 2H_2O$
UiO-66-(OH)$_2$|$_{8,2/12}$	$[Zr_6O_4(OH)_{7,8}(H_2O)_{3,8}(doBDC)_{4,1}]\cdot 2DMF$

Thermal stability of the samples was studied by powder X-ray thermo diffraction. According to the obtained thermo diffractograms (Figure S3), in samples UiO-66|$_{10/12}$ and UiO-66|$_{8,2/12}$ no evidence of degradation or phase transition is observed up to 450 °C and 375 °C, respectively, apart from a slightly shift of peak of UiO-66|$_{8,2/12}$ to higher 2θ angles (°) starting from 220 °C, which can be related to a contraction of the crystallographic structure due to the coordinated species release. However, in samples UiO-66-(OH)$_2$|$_{11/12}$ and UiO-66-(OH)$_2$|$_{8,2/12}$ thermal degradation was detected at 230 °C in case of UiO-66-(OH)$_2$|$_{11/12}$ and at 250 °C in case of UiO-66-(OH)$_2$|$_{8,2/12}$, by a decrease of peaks intensities and increase in their width. Moreover, an interesting phase transition was detected in sample UiO-66-

$(OH)_2|_{8,2/12}$ from 200 °C to 250 °C, which was not studied along the present work, as those temperatures were not reached during the experimental work.

In order to study the morphology of synthetized samples transmission electron microscopy (TEM) was performed (figure 4). TEM micrographs reveal that all samples consist of spherical particles. The particle size distribution depends on the synthetic procedure. Non defective samples (UiO-66$|_{10/12}$ and UiO-66-$(OH)_2|_{11/12}$) are obtained as MOF-gels consisting of small particles (average size are 10 nm and 15 nm, respectively). Several approaches were applied to disperse the nanoparticles of these gels form materials in order to study in more detail the particle size distribution. Nevertheless, due to this small size, the number of isolated particles identified by TEM was not enough to stablish a relevant particle size histogram. For defective samples, the incorporation of HCl modulator in the synthesis media induces particle growth. Thus, samples UiO-66$|_{8.2/12}$ and UiO-66-$(OH)_2|_{8.2/12}$ are formed by bigger and aggregated particles. Size range are 92(7) nm for sample UiO-66$|_{8.1/12}$ and 50(10) nm for UiO-66-$(OH)_2|_{8.2/12}$.

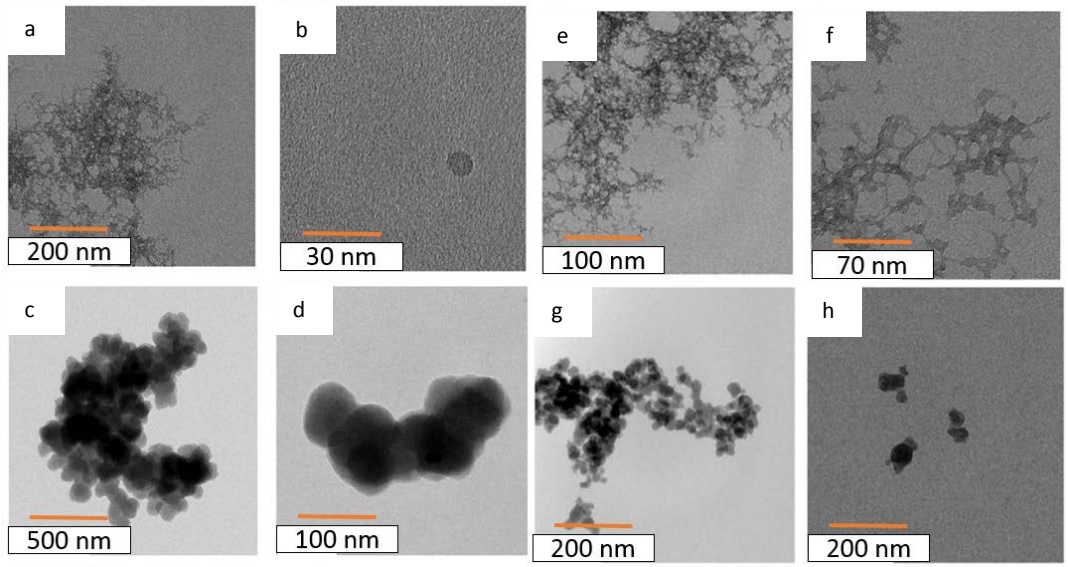

Figure 4. TEM micrographs of (a and b) UiO-66|$_{10/12}$, (c and d) UiO-66|$_{8.2/12}$, (e and f) UiO-66-(OH)$_2$|$_{11/12}$ and (g and h) UiO-66-(OH)$_2$|$_{8.2/12}$

β-alanine adsorption

Before performing the β-alanine adsorption tests, the total capacity of β-alanine in non-defective classical UiO-66 was calculated in order to set a reference for next assays. With that aim, the volume of β-alanine and pore volume of UiO-66|$_{12/12}$ was determined by Voronoi-Dirichlet polyhedral (VDP) approach [38] from the crystallographic information data of compounds (figure 5). Even if the VDP approach just gives information about the geometric volume of the cavities and target molecules, it has been used as it is a very effective approach to estimate molecular volumes from X-ray diffraction data. [39, 40]

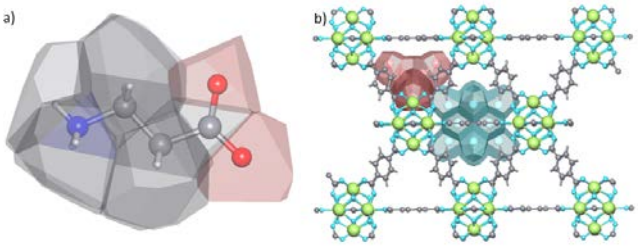

Figure 5. (a) Voronoi-Dirichlet polyhedral approach applied on β-alanine and view of the octahedral (blue) and tetrahedral (red) pores for UiO-66|$_{12/12}$

Based on Voronoi-Dirichlet polyhedral approach, the volume of β-alanine was estimated to be 100 Å^3; and the estimated volume of tetrahedral and octahedral cavities of UiO-66|$_{12/12}$ were 214 Å^3 and 421 Å^3, respectively. Moreover, as each cell unit presents 8 tetrahedral and 4 octahedral pores, the total volume of UiO-66|$_{12/12}$ per unit cell was estimated to be 3395 Å^3 per unit cell. Along this calculations the presence of any solvent was not taken into account; thus, the maximum capacity of UiO-66|$_{12/12}$ being less than 34 molecules per unit

cell or 6 molecules per formula units. That leads to a maximum theoretical adsorption capacity of 244 $mg_{\beta\text{-}Ala}/g_{UiO\text{-}66}$ in a non-defective standard UiO-66$|_{12/12}$ sample. Furthermore, if defects are introduced in the crystal structure (like in UiO-66$|_{8,1/12}$), bigger cavities are expected to be created, increasing the maximum β-alanine loading per unit cell. On the contrary, for UiO-66-$(OH)_2|_{12/12}$ the introduction of two hydroxyl groups is expected to have two opposite effects: 1) decrease of the volume of the octahedral and tetrahedral pores, and 2) increase of the host-guest interactions through hydrogen bonds.

In order to analyse the adsorption of β-alanine, MOF samples were dispersed in adsorbate aqueous solution and stirred. Afterwards, supernatant of the samples were analysed by HPLC-MS (figure 6).

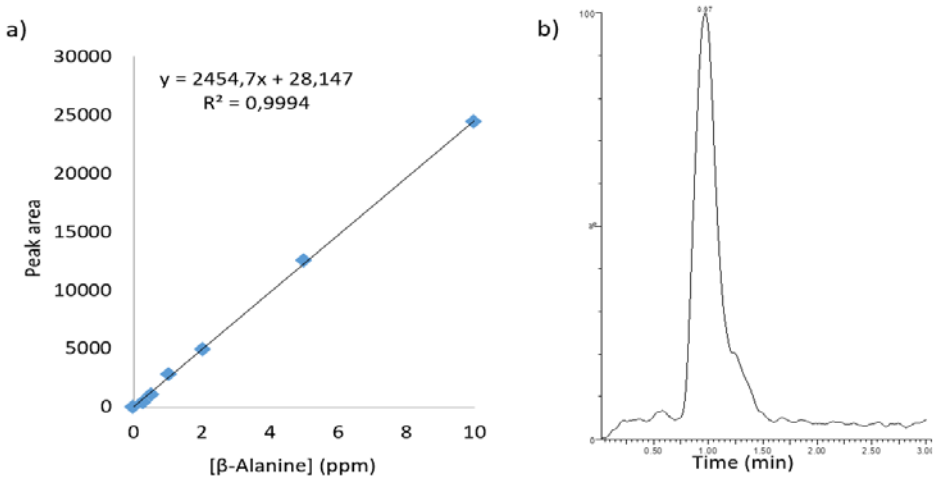

Figure 6. (a) Calibration curve and (b) chromatograph example of adsorption experiments supernatant for β-alanine obtained by HPLC/MS.

Quantification was performed with an external calibration (as it is explained in experimental section) containing target compound at concentrations ranging from 0.25 to 10 ppm in water. The samples were diluted in water for the analysis (final theoretical concentration around 1-2 ppm). The loaded β-alanine quantity (q_e) was calculated (equation 1) and adsorption isotherms was built (figure 7 (a)).

$$q\left(\frac{mg_{\beta-al}}{g_{UiO-66}}\right) = \frac{\Delta[\beta - al] \cdot V_{\beta-al\ solution}}{m_{UiO-66}} \qquad \text{(equation 1)}$$

where q= adsorption capacity of samples, $\Delta[\beta - al]$= difference between initial and final concentration of adsorbate in supernatant, $V_{\beta-al\ solution}$= volume of adsorbate solution used and m_{UiO-66}= used sample mass.

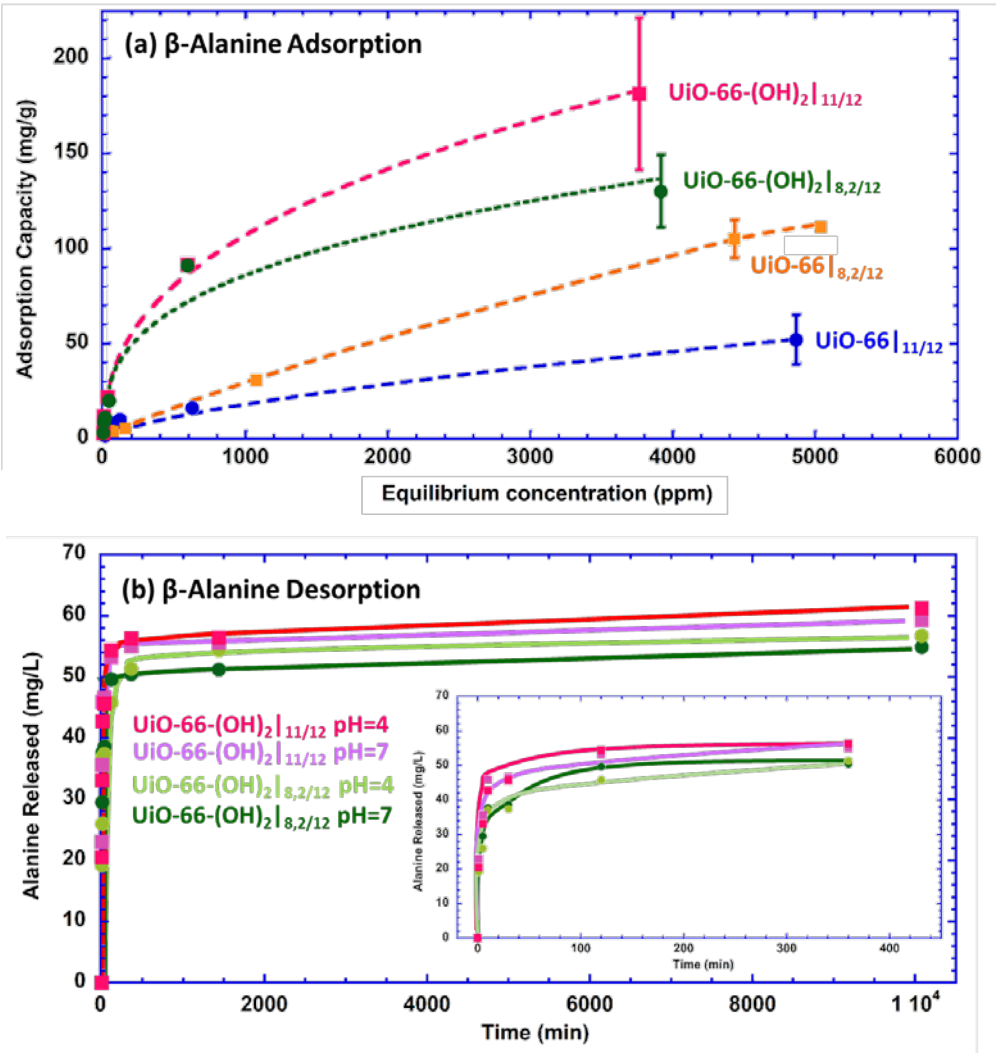

Figure 7. Adsorption and desortion of β-alanine (a) Adsorption values and Freundlich-simulated isotherms (doted lines) for samples UiO-66|$_{10/12}$, UiO-66|$_{8,2/12}$, UiO-66-(OH)$_2$|$_{11/12}$ and UiO-66-(OH)$_2$|$_{8,2/12}$ and (b) desorption values for UiO-66-(OH)$_2$|$_{11/12}$ and

UiO-66-$(OH)_2|_{8,2/12}$ samples at pH=7 and pH=4. Inset in b corresponds to the first 250 minutes.

As observed in figure 7(a), UiO-66-$(OH)_2|_{11/12}$ shows the higher capacity for β-alanine uptake, and UiO-66-$(OH)_2|_{10/12}$ the lower. The fact that the highest adsorption corresponds to UiO-66-$(OH)_2|_{11/12}$ confirms that the effect of the number of hydroxyl groups is more important than the pore volume. As mentioned before, the higher density of hydroxyl group, the better potential host-guest interaction through hydrogen bonds. Indeed, if the surface area was governing the adsorption capacity, it would be expected a higher β-alanine uptake for UiO-66$|_{11/12}$ (1067 cm^2/g) than for UiO-66-$(OH)_2|_{11/12}$ (397 m^2/g), but the opposite effect is observed in the obtained results [41]. Thus, this hypothesis was confirmed by the fact that adsorption capacity is higher for UiO-66-$(OH)_2|_{11/12}$ than for UiO-66-$(OH)_2|_{8.2/12}$. On the other hand, β-alanine uptake is higher for UiO-66$|_{8.2/12}$ than for UiO-66$|_{10/12}$. In the absence of further variables, this confirms that defective engineering promotes the adsorption by increasing the pore volume.

In order to study the affinity and adsorption capacity of the samples in a more precisely way, the isotherm data could be fitted according to Langmuir (equation 2) [42] and Freundlich models (equation 3) [43]. The main difference between them is that according to Langmuir model there is no chemical interaction between adsorbate and the adsorbent while according to Freundlich there is a chemical host-guest interaction.

$$\frac{[\beta - al]}{q} = \frac{1}{q_{max} \cdot K_L} + \frac{[\beta - al]}{q_{max}} \qquad \text{(equation 2)}$$

$$\ln q = \ln K_F + \frac{1}{n} \cdot \ln[\beta - al] \qquad \text{(equation 3)}$$

where [β-al] is the initial concentration of β-alanine in the solution; q_{max} is the capacity of adsorption, q_{max} is the maximum capacity of adsorption, and K_L is the Langmuir constant, and K_F and n are the Freundlich constant and exponent, respectively.

The attempts to fit the experimental data to Langmuir model were unsuccessful. However, Freundlich model was applied to the four compounds (figure S4). Even if the goodness of the fit for UiO-66-$(OH)_2|_{8,2/12}$ is lower than for the rest of the samples, the fitting confirms the occurrence of chemical host-guest interactions. The as-obtained values for K_f and n can be seen in table 2.

Table 2. Freundlich constant (K_F in mg of adsorbate per g of host framemork) and exponent inverse (1/n) for the adsorption of β-alanine.

MOF	K_F (mg·g^{-1})	1/n
UiO-66$|_{10/12}$	0.6725	0.5197
UiO-66$|_{8,2/12}$	0.3327	0.6859
UiO-66-$(OH)_2|_{11/12}$	5.2677	0.4354
UiO-66-$(OH)_2|_{8,2/12}$	4.8187	0.4207

Comparison of K_F values shows that the absorption capacity increases significantly with the presence of hydroxyl groups. All the 1/n values are lower than 1 conforming chemisorption process. According to Foo and Hameed [44], a little percentage of β-alanine could be covalently bonded to the defective positions of the zirconium hexanuclear clusters, while most of it is expected tobe anchored through weak interactions such as hydrogen bonding. On the hand, the n values show that in all the cases affinity for β-alanine is quite similar, but a slightly higher for compounds exhibiting doBDC ligands, which again confirms the favourable effect of the hydroxyl groups as anchoring points. K_F and n values are expected

to be higher for UiO-66|$_{8.2/12}$ than for UiO-66|$_{10/12}$ but they are not. The reason can be found in the fact that, as previously mentioned, Freundlich fitting for UiO-66|$_{8.2/12}$. is poor (R^2=0.8915).

Characterization of β-alanine-loaded samples

XRD was performed over β-alanine-loaded samples (Figure S5) in order to study its structural stability after the adsorption process. With that aim, samples loaded with a high β-alanine concentration (≈ 10000 ppm) were centrifuged after the adsorption process and dried at 80 ^{o}C for 2 days. The results confirm that structural integrity is kept.

In order to verify the presence of β-alanine, IR spectroscopy was also performed over the loaded samples, and compared with the data obtained from activated samples. With this aim, KBr pellet of loaded samples were prepared (1% (w/w) concentration) and dried in the oven at 100 °C for 48 h, to ensure that adsorbed water was eliminated, obtaining clearer IR spectra. Moreover, IR spectra was also performed (KBr pellet concentration 0.5% (w/w)) on pure β-alanine (Figure S6 and table S6). The most significant signal confirming the presence of β-alanine corresponds to the amine group (-NH_2). In addition, the removal of DMF in the activated samples was confirmed by the absence of the band at approximately 1660 cm^{-1} assigned to $\nu(C=O)_{Stretch}$.

The amount of adsorbed β-alanine was determined by combining data from elemental (figure S7) and thermogravimetric analysis (figure S8). The total amount of nitrogen detected by EA was ascribed to the β-alanine uptake, and the fact that it is lower for loaded structures in the case of UiO-66-$(OH)_2$|$_{11/12}$ and (d) UiO-66-$(OH)_2$|$_{8,2/12}$ is explained by considering that, during the β-alanine adsorption, water is also adsorbed. Despite special care was taken to dry the samples after the EA analyses, samples are able to capture moisture from the environment. So, as the hydration degree in the formulae affects the

calculated C, N and H percentages, the discrepancies found for the amount of the β-alanine calculated from adsorption and EA-TGA combined analyses are explained.

Figure S8 reveals clear differences in the mass loss associated to the coordinated ligands and the crystallisation molecules (150 ^{o}C-350 ^{o}C), and during the ligand calcination stage (above 350 ^{o}C). The total mass loss is clearly higher for the β-alanine loaded samples, as expected. The mass loss at intermediate temperatures clearly indicates that the β-alanine molecules are of crystallisation-type. Thus, table 3 summarizes the calculated number of crystallisation molecules per cluster for unloaded and loaded samples [41, 45, 46].

Table 3. Description of main chemical characteristics of the unloaded and β-alanine loaded samples: Number of crystallisation molecules per cluster for unloaded (before activation) and alanine and water molecules for loaded samples obtaind from the combination of TGA and EA analyses. Surface area, particle size, and alanine adsorption capacities determined by adsorption isotherms ($q_{(IT)}$) and elemental analyses ($q_{(FA)}$).

MOF	Before activation		Surface Area	Particle Size	Loaded samples		β-alanine loading (mg/g)	
	DMF	H_2O	(m^2/g)	(nm)	β-alanine	H_2O	$q_{(IT)}$	$q_{(FA)}$
UiO-66|$_{10/12}$	1.5	6.5	1067	< 20	2.2	12	51	99
UiO-66|$_{8.2/12}$	0.75	5	1400	92(7)	2.1	20	116	92
UiO-66-$(OH)_2$|$_{11/12}$	3.25	2	396	< 20	3.7	8	181	149
UiO-66-$(OH)_2$|$_{8.2/12}$	2	0	550	50(10)	3.2	6.5	128	142

Particle size has been calculated from TEM
Data not corresponding to this work have been obtained for references [41, 45, 46].

As mentioned before, the calculated maximum capacity per cluster has been calculated to be six molecules of β-alanine for ideal UiO-66|$_{12/12}$. Therefore, values higher than 35% of the ideal one must be positively considered. In general, the results are in good agreement with the conclusions made from adsorption isotherms (figure 7 (a)), showing a higher alanine uptake by the hydroxyl samples, and lower affinity for the non-functionalized materials. Despite the adsorption isotherms suggest qualitative difference between the β-alanine uptake of non-defective and defective samples; this tendency does not agree completely with the data obtained from elemental analyses. It is worth considering that in addition to the added to the experimental uncertainty for high concentrations, the hydration produce further uncertainty. Therefore, the obtained results need to be interpreted carefully.

Table 4 shows several adsorption capacity values for MOF-type UiO-66 and derivatives corresponding to different adsorbates. From the studied data, the highest value is 408 mg of sulfachloropyridazine per g of UiO-66 [47]. In relation to the derivatives, UiO-66-COOH-1 MOF has been reported to adsorb 476.4 mg of congo red per g [48]. Comparison of data in tables 3 and 4 indicate similar adsorption capacity for β-alanine and **i**buprofen. However, values for naproxen are slightly lower [49]. Ibuprofen (206.285 g·mol^{-1}) and naproxen (230.263 g·mol^{-1}) have similar size but the latter is less polar.

Table 4. Adsorption capacity values for MOF-type UiO-66 and derivatives corresponding to different adsorbates

Adsorbate	adsorption capacity (mg/g)	MOF	reference
SCP**, 5 mg/L	50	UiO-66	[47]
SCP**, 25 mg/L	221	UiO-66	
SCP**, 45 mg/L	408	UiO-66	
SCP**	403	UiO-66, 273 K	
SCP**	339	UiO-66, 283 K	
SCP**	312	UiO-66, 293 K	
methylene blue	165.9	UiO-66-COOH-1	[48]
methylene blue	197.7	UiO-66-COOH-2	
methylene blue	157.5	UiO-66-COOH-3	
congo red	476.4	UiO-66-COOH-1	
congo red	401.1	UiO-66-COOH-2	
congo red	395.9	UiO-66-COOH-3	
ibuprofen	127.1	UiO-66	[49]
ibuprofen	50.69	UiO-66-NH_2	
naproxen	88.51.	UiO-66	
naproxen	40.10	UiO-66-NH_2	
methyl orange	84.8	UiO-66	[50]
congo red	13.2	UiO-66	
methylene blue	70.4	UiO-66	
rhodamine	67.5	UiO-66	
rhodamine, 273K	53.307	UiO-66	[51]
rhodamine, 303K	70.679	UiO-66	

*adsorption capacity in mg of adsorbate per g of UiO-66 or derivative MOF
**SCP is sulfachloropyridazine

Desorption of β-alanine

Figure 7 (b) shows the amount of β-alanine released after 7 days from 100 mg of UiO-66-$(OH)_2|_{11/12}$ and UiO-66-$(OH)_2|_{8,2/12}$. Samples were charged in 5000 ppm adsorbate solution (100 mL of water). Experiments were carried out at pH values of 4 and 7. As observed, the majority of the β-alanine is released in the first 200 minutes of the experiment. Afterwards a slight increase of the adsorbate`s concentration is detected.

Acidity of the media has a negligible effect on the β-alanine release for defective samples UiO-66-$(OH)_2|_{11/12}$ and UiO-66-$(OH)_2|_{8,2/12}$ Despite the initial β-alanine loading is higher on the non-defective hydroxylated material, the amount and kinetics of alanine release is similar for defective and non-defective samples. Therefore, the maximum adsorption capacity is not the unique parameter driven the desorption efficiency.

More interesting is that the release of loaded β-alanine molecules is not complete in any of the studies cases, since starting from loading values of 180 mg/g to 120 mg/g for UiO-66-$(OH)_2|_{11/12}$ and UiO-66-$(OH)_2|_{8,2/12}$ materials, only 60 to 50 mg/g are released to the aqueous media. Even taking into consideration the uncertainties of the experimental procedures, between 140 and 60 mg/g of β-alanine could remain within the UiO-66-$(OH)_2|_{11/12}$ and UiO-66-$(OH)_2|_{8,2/12}$ structures after the desorption process.

Considering all the experimental evidences jointly, it can be concluded that, at low β-alanine concentrations, hydroxyl derivative samples exhibit a greater affinity for the amino acid; being this affinity ascribed to weak interactions between the host and guest structures. The most probable interactions ascribed to hydrogen bonding between hydroxyl – carboxyl and hydroxyl – amine bridges. For higher β-alanine concentrations, a second type of adsorbate chemisorption could take place, such as the alanine covalent anchoring to the defect positions of the zirconium hexa-nuclear clusters [52]. This strong bonding

could explain the resistance of β-alanine to be desorbed in the conditions that have been explored during this work. Nevertheless, the β-alanine loading on UiO66-$(OH)_2$ frameworks after the desorption means that between 2.0 (UiO-66-$(OH)_2|_{8,2/12}$) to 3.0 (UiO-66-$(OH)_2|_{11/12}$) molecules are capping the defective position of the clusters, which is possible for the defective UiO-66-$(OH)_2|_{8,2/12}$ material, but not for the UiO-66-$(OH)_2|_{11/12;}$ since its structure only exhibits one functionalizable position. Nevertheless, the chemical lability of these materials can explain the fact that linker exchange occurs without disturbing their crystal structure [53]. Therefore, adsorption and desorption capacity of UiO-66-$(OH)_2|_{11/12}$ material could be explained based on a combination of adsorption, defect position capping and H_2doBDC organic linker displacement by β-alanine.

5. CONCLUSIONS

Taking into consideration the experimental uncertainties of the experimental methodologies, it can be clearly stated that the hydroxyl functionalized frameworks have more chemical affinity and capacity to adsorb β-alanine than non-functionalized UiO-66 frameworks. Adsorption isotherms suggest that defect engineering could provoke enhancing or detrimental effect on β-alanine uptake in UiO66-$(OH)_2$ and UiO66 materials, respectively. Nevertheless, the uncertainty of the adsorption isotherm data at high concentration, and the mismatch with the β-alanine loading obtained from elemental analysis, makes this tendency not conclusive. Desorption tests on UiO66-$(OH)_2$ materials indicate that an important percentage of the β-alanine (from one to three molecules) remain in the material after the process; which clearly points toward a two types of host-guess interactions, weak interacting β-alanine species located at the pores, and covalently bonded amino acid molecules bonded to the zirconium clusters of the materials. Further

work is ongoing to clarify if a combination of cluster capping and ligand displacement is responsible of this effect.

Acknowledgments

The following funding is acknowledged: Ministerio de Economía y Competitividad [MAT2016-76739-R (AEI/FEDER, UE); Universidad del País Vasco/ Euskal Herriko Unibertsitatea (GIU 18/197). ELKARTEK-ACTIMAT, HAZITEK-SIMAN and PIBA-LIMOFILM (PIBA-2018-06).

References

[1] F. Gándara, T. D. Bennett, Crystallography of Metal-Organic Frameworks, IUCrJ. 1 (2014) 563–570. https://doi.org/10.1107/S2052252514020351.

[2] C. V. McGuire, R. S. Forgan, The Surface Chemistry of Metal–organic Frameworks, Chem. Commun. 51 (2015) 5199–5217. https://doi.org/10.1039/c4cc04458d.

[3] S. Begum, Z. Hassan, S. Braese, C. Woell, M. Tsotsalas, Metal-Organic Framework-Templated Biomaterials: Recent Progress in Synthesis, Functionalization, and Applications, Acc. Chem. Res. 52 (2019) 1598-1610. https://doi.org/10.1021/acs.accounts.9b00039.

[4] Z. Hasan, S. H. Jhung, Removal of Hazardous Organics from Water Using Metal-Organic Frameworks (MOFs): Plausible Mechanisms for Selective Adsorptions, J. Hazard. Mater. 283 (2015) 329–339. https://doi.org/10.1016/j.jhazmat.2014.09.046.

[5] P. Horcajada, R. Gref, T. Baati, P. K. Allan, G. Maurin, P. Couvreur, G. Férey, R. E. Morris, C. Serre, Metal-Organic Frameworks in Biomedicine. Chem. Rev. 112 (2012) 1232–1268. https://doi.org/10.1021/cr200256v.

[6] J. Della Rocca, D. Liu, W. Lin, Nanoscale Metal-Organic Frameworks for Biomedical Imaging

and Drug Delivery, Acc. Chem. Res, 44 (2010) 957–968. https://doi.org/10.1021/ar200028a.

[7] M. Giménez-Marqués, T. Hidalgo, C. Serre, P. Horcajada, Nanostructured Metal-Organic Frameworks and Their Bio-Related Applications. Coord. Chem. Rev. 307 (2016) 342–360. https://doi.org/10.1016/j.ccr.2015.08.008.

[8] I. Imaz, M. Rubio-Martínez, J. An, I. Solé-Font, N. L. Rosi, D. Maspoch, Metal–biomolecule Frameworks (MBioFs). Chem. Commun. 47 (2011) 7287–7302. https://doi.org/10.1039/C1CC11202C.

[9] H. Furukawa, F. Gándara, Y.-B. Zhang, J. Jiang, W. L. Queen, M. R. Hudson, O. M. Yaghi, Water Adsorption in Porous Metal–Organic Frameworks and Related Materials, J. Am. Chem. Soc. 136 (2014) 4369–4381. https://doi.org/10.1021/ja500330a.

[10] X. Gao, X. Hai, H. Baigude, W. Guan, Z. Liu, Fabrication of Functional Hollow Microspheres Constructed from MOF Shells: Promising Drug Delivery Systems with High Loading Capacity and Targeted Transport. Sci. Rep. 6 (2016) 1–10. https://doi.org/10.1038/srep37705.

[11] P. Horcajada, C. Serre, M. Vallet-Regí, M. Sebban, F. Taulelle, G. Férey, MOFs as Efficient Materials for Drug Delivery, Angew. Chem. (2006) 6120–6124. https://doi.org/10.1002/anie.200601878.

[12] M. Vallet-Regí, F. Balas, D. Arcos, Mesoporous Materials for Drug Delivery, Angew. Chemie Int. Ed. 46 (2007) 7548–7558. https://doi.org/10.1002/anie.200604488.

[13] J. H. Cavka, S. Jakobsen, U. Olsbye, N. Guillou, Carlo Lamberti, S. Bordiga, K. P. Lillerud, A New Zirconium Inorganic Building Brick Forming Metal Organic Frameworks with Exceptional Stability, J. Am. Chem. Soc. 6 (2008) 1–19. https://doi.org/10.1021/ja8057953.

[14] M. E. Cass, T. M. Garrett, K. N. Raymond K. N. The Salicylate Mode of Bonding in Protonated Ferric Enterobactin Analogues. J. Am. Chem. Soc. 111 (1989) 1677–1682. https://doi.org/10.1021/ja00187a021.

[15] K. N. Raymond, B. E. Allred, and A. K. Sia, Coordination Chemistry of Microbial Iron

Transport, Acc Chem Res. 48(9) (2015) 2496–2505. https://doi.org/10.1021/acs.accounts.5b00301.

[16] A. Koutsianos, E. Kazimierska, A. R. Barron, M. Taddei, E. Andreoli, A new approach to enhancing the CO_2 capture performance of defective UiO-66 via post-synthetic defect exchange, Dalton Trans. 48 (2019) 3349-3359. https://doi.org/10.1039/C9DT00154A.

[17] M. Taddei, R. J. Wakeham, A. Koutsianos, E. Andreoli, A. R. Barron, Post-Synthetic Ligand Exchange in Zirconium-Based Metal–Organic Frameworks: Beware of The Defects!, Angew. Chem .Int. Ed. 57, (2018) 11706–11710. https://doi.org/10.1002/anie.201806910.

[18] Y. Han, M. Liu, K. Li, Y. Zuo, Y. Wei, S. Xu, G. Zhang, C. Song, Z. Zhang, X. Guo, Facile Synthesis of Morphology and Size-Controlled Zirconium Metal–organic Framework UiO-66: The Role of Hydrofluoric Acid in Crystallization. CrystEngComm 17 (2015) 6434–6440. https://doi.org/10.1039/C5CE00729A.

[19] Y. Jiao, Y. Liu, G. Zhu, J.T. Hungerford, S. Bhattacharyya, R.P. Lively, D.S. Sholl, K.S. Walton, Heat-Treatment of Defective UiO-66 from Modulated Synthesis: Adsorption and Stability Studies, J. Phys. Chem. C. 121 (2017) 23471-23479. https://doi.org/10.1021/acs.jpcc.7b07772.

[20] S. Lin, J.K. Bediako, M.H. Song, J.A. Kim, C.W. Cho, Y. Zhao, J.W. Choi, Y.S. Yun, Effective Recovery of Pt(IV) from Acidic Solution by a Defective Metal-Organic Frameworks Using Central Composite Design for Synthesis, ACS Sustainable Chemistry & Engineering 7 (2019) 7510-7518. https://doi.org/10.1021/acssuschemeng.8b04637.

[21] W. P. Lustig, S. Mukherjee, N. D. Rudd, A. V. Desai, J. Li, S. K. Ghosh, Metal–organic Frameworks: Functional Luminescent and Photonic Materials for Sensing Applications, Chem.Soc.Rev. 46 (2017) 3242–3285. https://doi.org/1039/C6CS00930A

[22] Z. Fang, B. Bueken, D. E. De Vos, R. A. Fischer, Defect-Engineered Metal-Organic Frameworks, Angew. Chemie-Int.Ed. 54 (2015) 7234–7254. https://doi.org/

10.1002/anie.201411540

[23] W. Liang, C. J. Coghlan, F. Ragon, M. Rubio-Martinez, D. M. D'Alessandro, R. Babarao, Defect Engineering of UiO-66 for CO_2 and H_2O Uptake – a Combined Experimental and Simulation Study, Dalton. Trans. 45 (2016) 4496–4500. https://doi.org/ 10.1039/C6DT00189K

[24] M. J. Katz, Z. J. Brown, Y. J. Colón, P. W. Siu, K. A. Scheidt, R. Q. Snurr, J. T. Hupp, O. K. Farha, A Facile Synthesis of UiO-66, UiO-67 and Their Derivatives, Chem. Commun. 49 (2013) 9449-9451. https://doi.org/ 10.1039/C3CC46105J.

[25] G. C. Shearer, S. Chavan, J. Ethiraj, J. G. Vitillo, S. Svelle, U. Olsbye, C. Lamberti, S. Bordiga, K. P. Lillerud, Tuned to Perfection: Ironing Out the Defects in Metal–Organic Framework UiO-66, Chem. Mater. 26 (2014) 4068–4071, https://doi.org/10.1021/cm501859p

[26] L. L. Tan, H. Li, Y. Zhou, Y. Zhang, X. Feng, B. Wang, Y. W. Yang, Zn(2+)-Triggered Drug Release from Biocompatible Zirconium MOFs Equipped with Supramolecular Gates, Small, 11 (2015) 3807–3813. https://doi.org/10.1002/smll.201500155.

[27] Y. Han, M. Liu, K. Li, Y. Zuo, Y. Wei, S. Xu, G. Zhang, C. Song, Z. Zhang, X. Guo, Facile Synthesis of Morphology and Size-Controlled Zirconium Metal–organic Framework UiO-66: The Role of Hydrofluoric Acid in Crystallization, CrystEngComm 17 (2015) 6434–6440. https://doi.org/10.1039/C5CE00729A.

[28] M. Nazari, M. Rubio-Martinez, G. Tobias, J. P. Barrio, R. Babarao, F. Nazari, K. Konstas, B. W. Muir, S. F. Collins, A. J. Hill, Metal-Organic-Framework-Coated Optical Fibers as Light-Triggered Drug Delivery Vehicles, Adv. Funct. Mater. 26 (2016) 3244–3249. https://doi.org/10.1002/adfm.201505260

[29] D. Cunha, C. Gaudin, I. Colinet, P. Horcajada, G Maurin, C. Serre, Rationalization of the Entrapping of Bioactive Molecules into a Series of Functionalized Porous Zirconium Terephthalate MOFs, J. Mater. Chem. B, 1 (2013) 1101-1111.

https://doi.org/10.1039/C2TB00366J

[30] P. Horcajada, T. Chalati, C. Serre, B. Gillet, C. Sebrie, T. Baati, J. F. Eubank, D. Heurtaux, P. Clayette, C. Kreuz, Porous Metal-Organic-Framework Nanoscale Carriers as a Potential Platform for Drug Delivery and Imaging, Nat. Mater. 9 (2010) 172–178. https://doi.org/10.1038/nmat2608.

[31] H. Furukawa, F. Gándara, Y-B. Zhang, J. Jiang, W. L. Queen, M. R. Hudson, O. M. Yaghi, Water Adsorption in Porous Metal–Organic Frameworks and Related Materials, J. Am. Chem. Soc., 136 (2014) 4369-4381, https://doi.org/10.1021/ja500330

[32] W. Derave, M. S. Ozdemir, R. C. Harris, A. Pottier, H. Reyngoudt, K. Koppo, J. A. Wise, E. Achten, β-alanine supplementation augments muscle carnosine content and attenuates fatigue during repeated isokinetic contraction bouts in trained sprinters, J. Appl. Physiol. 103 (2007) 1736–1743. https://doi.org/10.1152/japplphysiol.00397.2007

[33] L. Blancquaert, S. P. Baba, S. Kwiatkowski, J. Stautemas, S. Stegen, S. Barbaresi, W. Chung, A.A. Boakye, J. D. Hoetker, A. Bhatnagar, J. Delanghe, B. Vanheel, M. Veiga-da-Cunha, W. Derave, I. Everaert, Carnosine and anserine homeostasis in skeletal muscle and heart is controlled by β-alanine transamination, J. Physiol. 594 (2016) 4849-63. https://doi.org/ 10.1113/JP272050

[34] S. Stegen, L. Blancquaert, I. Everaert, T. Bex , Y. Taes, P. Calders, E. Achten, W. Derave, Meal and beta-alanine coingestion enhances muscle carnosine loading, Med. Sci.Sports Exerc. 45 (2013) 1478–1485. https://doi.org/10.1249/MSS.0b013e31828ab073.

[35] A. Pihl, P. Fritzson, The catabolism of C14-labeled β-alanine in the intact rat., J. Biol. Chem. 215 (1955) 345–351.

[36] C. A. Hill, R. C. Harris, H. J. Kim, B. D. Harris, C. Sale, L- H. Boobis, C. K. Kim, J. A. Wise, Influence of beta-alanine supplementation on skeletal muscle carnosine concentrations and high intensity cycling capacity, Amino Acids 32 (2007) 225–233.

https://doi.org/10.1007/s00726-006-0364-4.

[37] J. Rodriguez-Carvajal, Recent developments of the program FullProf, IUCr Newsletter, 26 (2001) 12-19.

[38] V. A. Blatov, A. P. Shevchenko, V. N. Serenzhkin, Crystal space analysis by means of Voronoi–Dirichlet polyhedra, Acta Crystallogr. Sect. A. 51 (1995) 909–916. https://doi.org/10.1107/S0108767395006799.

[39] V. A. Blatov, Voronoi–dirichlet polyhedra in crystal chemistry: theory and applications, Crystallography Reviews, 10 (2004), 249-318. https://doi.org/10.1080/08893110412331323170

[40] V. A. Blatov, A. P. Shevchenko (2003), Analysis of voids in crystal structures: the methods of `dual' crystal chemistry, Acta Crystallographica Section A (Foundations and Advances) , 59 (2003) 34-44. https://doi.org/10.1107/S0108767302020603.

[41] Z. H. Rada, H. R. Abid, J. Shang, H. Sun, Y. He, P. Webley, S. Liu, S. Wang, Functionalized UiO-66 by single and binary $(OH)_2$ and NO_2 groups for uptake of CO_2 and CH_4, Ind. Eng. Chem. Res. 55 (2016) 7924–7932. https://doi.org/10.1021/acs.iecr.5b04061.

[42] I. Langmuir, The adsorption of gases on plane surfaces of glass, mica and platinum, J. Am. Chem. Soc. 40 (1918) 1361–1403. https://doi.org/10.1021/ja02242a004.

[43] R. Sips, On the structure of a catalyst surface, J. Chem. Phys. 16 (1948) 490–495. https://doi.org/10.1063/1.1746922.

[44] K. Y. Foo, B. H. Hameed, Insights into the modeling of adsorption isotherm systems, Chemical Engineering Journal, 156 (2010) 2-10, https://doi.org/10.1016/j.cej.2009.09.013

[45] Z. Wang, J. Yang, Y. Li, Q. Zhuang, J. Gu, Simultaneous degradation and removal of CrVI from aqueous solution with Zr-based Metal–Organic Frameworks bearing inherent reductive sites. Chem. Eur. J. 23 (2017) 15415–15423. https://doi.org/10.1002/chem.201702534.

[46] M. J. Katz, Z. J. Brown, Y. J. Colón, P. W. Siu, K. A. Scheidt, R. Q. Snurr, J. T. Hupp, O. K. Farha,

A facile synthesis of UiO-66, UiO-67 and their derivatives, Chem. Commun., 49 (2013) 9449-9451. https://doi.org/ 10.1039/C3CC46105J.

[47] X. Zhang, X. Lv, X. Shi, Y. Yang, Y. Yang, Enhanced hydrophobic UiO-66 (University of Oslo 66) metal-organic framework with high capacity and selectivity for toluene capture from high humid air, J.Colloid Interface Sci. 539 (2019) 152–160. https://doi.org/10.1016/j.jcis.2018.12.056.

[48] W. Zhang, J.-M. Yang, R.-N. Yang, B.-C. Yang, S. Quan, X. Jiang, Effect of free carboxylic acid groups in UiO-66 analogues on the adsorption of dyes from water: Plausible mechanisms for adsorption and gate-opening behaviour, J. Mol. Liq. 283 (2019) 160–166. https://doi.org/10.1016/j.molliq.2019.03.100/

[49] W. Sun, H. Li, H. Li, S. Li, X. Cao, Adsorption mechanisms of ibuprofen and naproxen to UiO-66 and UiO-66-NH2: Batch experiment and DFT calculation, Chemical. Eng. J. 360 (2019) 645-653. https://doi.org/10.1016/j.cej.2018.12.021.

[50] J. Qiu, Y. Feng, X. Zhang, M. Jia, J. Yao, Acid-promoted synthesis of UiO-66 for highly selective adsorption of anionic dyes: Adsorption performance and mechanisms, J. Colloid Interface Sci. 499 (2017) 151–158. https://doi.org/10.1016/j.jcis.2017.03.101.

[51] Q. He, Q Chen, M. Lü, X. Liu, Adsorption behavior of rhodamine B on UiO-66, Chin. J. Chem. Eng. 22 (2014) 1285-1290. https://doi.org/10.1016/j.cjche.2014.09.009.

[52] A. Koutsianos, E. Kazimierska, A. R. Barron, M. Taddei, E. Andreoli, A new approach to enhancing the CO_2 capture performance of defective UiO-66 via post-synthetic defect exchange, Dalton Trans. 48 (2019) 3349-3359. https://doi.org/10.1039/C9DT00154A.

[53] M. Taddei, R. J. Wakeham, A. Koutsianos, E. Andreoli, A. R. Barron, Post-Synthetic Ligand Exchange in Zirconium-Based Metal–Organic Frameworks: Beware of The Defects!, Angew. Chem. Int. Ed. 57, (2018) 11706–11710. https://doi.org/10.1002/anie.201806910

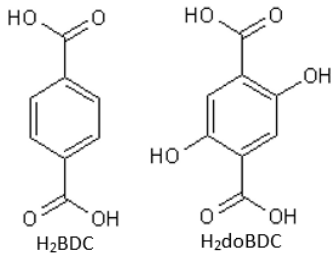

Figure 1. Organic linkers H_2BDC (1,4-benzenedicaboxylic acid) and H_2doBDC (2,5-dihydroxy-1,4-benzenedicarboxylic acid)

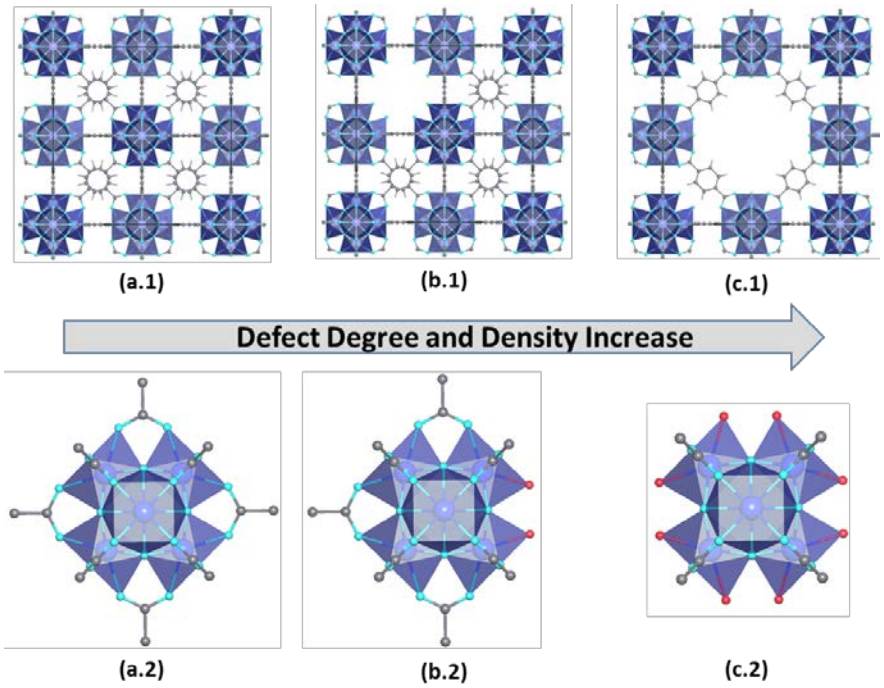

Figure 2. (a.1) and (a.2) Ideal UiO-66 crystal structure and 12-c zirconium hexameric clusters. Detail of (b.1) Ligand defect and (c.1) cluster defects within the UiO-66 framework. (b.2) Representation of possible local structures for nearly ideal 11/12 connected non defective and (c.2) 8/12 defective zirconium clusters. Zirconium atoms are coloured in dark blue, oxygen in light blue and carbon in grey. Red spheres indicate coordinated species for charge neutrality and saturation of coordination environment.

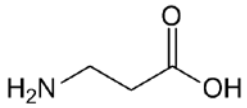

Figure 3. Structure of β-alanine.

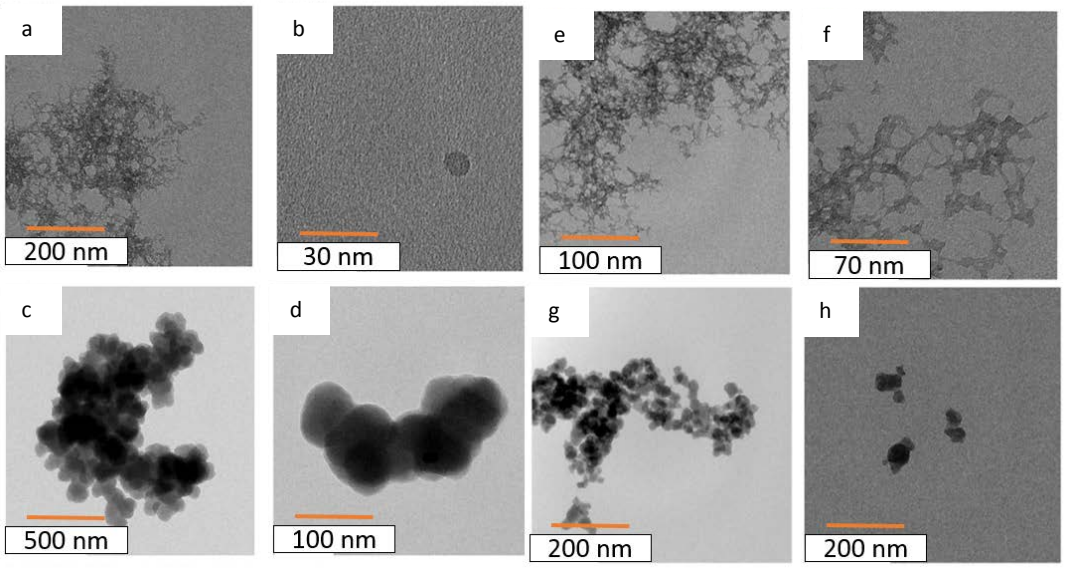

Figure 4. TEM micrographs of (a and b) UiO-66|$_{10/12}$, (c and d) UiO-66|$_{8'2/12}$, (e and f), UiO-66-(OH)$_2$|$_{11/12}$ and (g and h) UiO-66-(OH)$_2$|$_{8'2/12}$

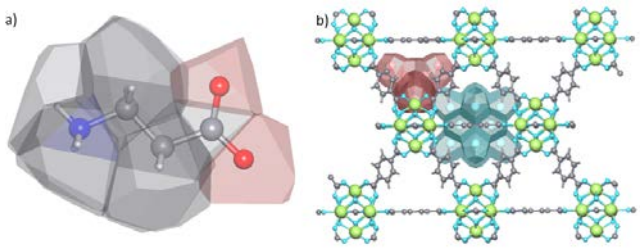

Figure 5. (a) Voronoi-Dirichlet polyhedral approach applied on β-alanine and view of the octahedral (blue) and tetrahedral (red) pores for UiO-66|$_{12/12}$

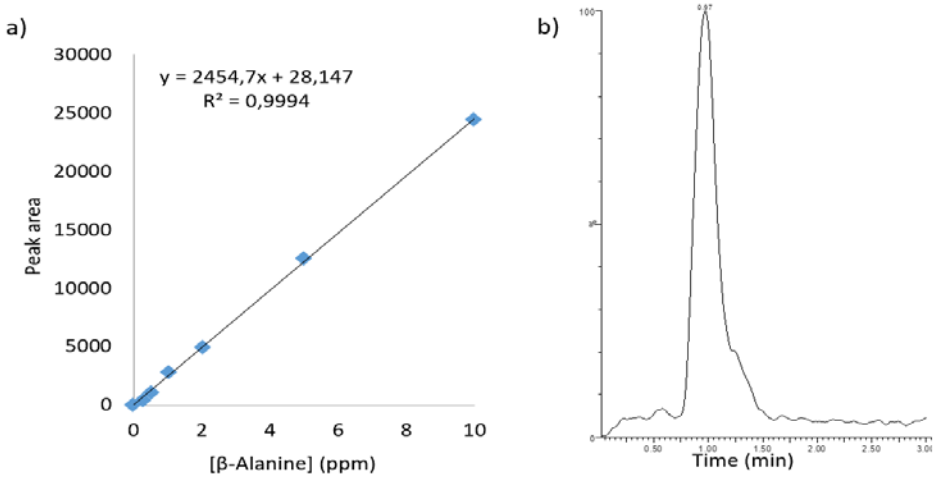

Figure 6. (a) Calibration curve and (b) chromatograph example of adsorption experiments supernatant for β-alanine obtained by HPLC/MS.

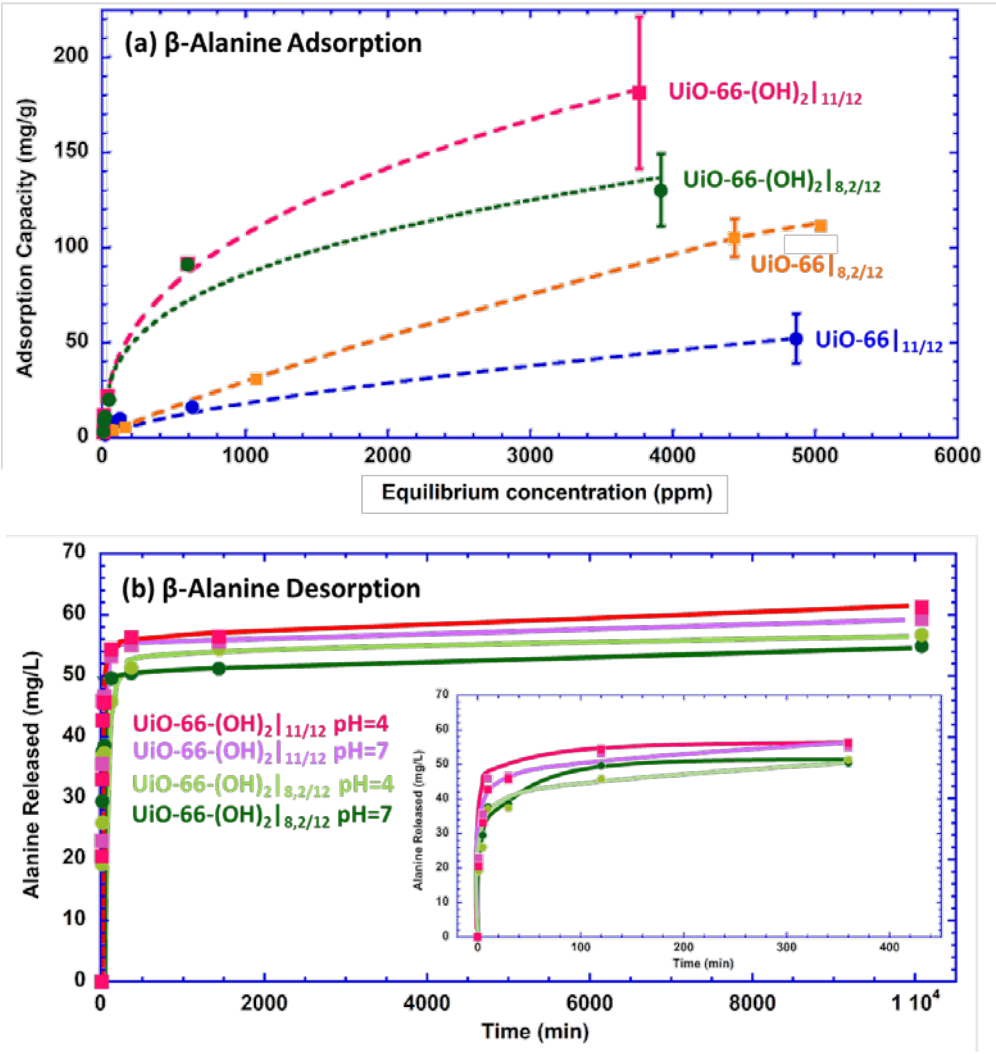

Figure 7. Adsorption and desortion of β-alanine (a) Adsorption values and Freundlich-simulated isotherms (doted lines) for samples UiO-66|$_{10/12}$, UiO-66|$_{8,2/12}$, UiO-66-(OH)$_2$|$_{11/12}$ and UiO-66-(OH)$_2$|$_{8,2/12}$ and (b) desorption values for UiO-66-(OH)$_2$|$_{11/12}$ and UiO-66-(OH)$_2$|$_{8,2/12}$ samples at pH=7 and pH=4. Inset in b corresponds to the first 250 minutes.

Table 1. Chemical formula for raw materials

Compound	**Chemical formula**
UiO-66|$_{10/12}$	$[Zr_6O_4(OH)_6(H_2O)_2(BDC)_5]\cdot 1.5DMF\cdot 6.5H_2O$
UiO-66|$_{8,2/12}$	$[Zr_6O_4(OH)_{7,8}(H_2O)_{3,8}(BDC)_{4,1}]\cdot 0.75DMF\cdot 5H_2O$
UiO-66-$(OH)_2$|$_{11/12}$	$[Zr_6O_4(OH)_5(H_2O)(doBDC)_{5,5}]\cdot 3.25DMF\cdot 2H_2O$
UiO-66-$(OH)_2$|$_{8,2/12}$	$[Zr_6O_4(OH)_{7,8}(H_2O)_{3,8}(doBDC)_{4,1}]\cdot 2DMF$

Table 2. Freundlich constant (K_F in mg of adsorbate per g of host framemork) and exponent inverse (1/n) for the adsorption of β-alanine.

MOF	K_F ($mg \cdot g^{-1}$)	1/n
UiO-66|$_{10/12}$	0.6725	0.5197
UiO-66|$_{8,2/12}$	0.3327	0.6859
UiO-66-$(OH)_2$|$_{11/12}$	5.2677	0.4354
UiO-66-$(OH)_2$|$_{8,2/12}$	4.8187	0.4207

Table 3. Description of main chemical characteristics of the unloaded and β-alanine loaded samples: Number of crystallisation molecules per cluster for unloaded (before activation) and alanine and water molecules for loaded samples obtaind from the combination of TGA and EA analyses. Surface area, particle size, and alanine adsorption capacities determined by adsorption isotherms ($q_{(IT)}$) and elemental analyses ($q_{(FA)}$).

MOF	Before activation		Surface Area	Particle Size	Loaded samples		β-alanine loading (mg/g)	
	DMF	H_2O	(m^2/g)	(nm)	β-alanine	H_2O	$q_{(IT)}$	$q_{(FA)}$
UiO-66|$_{10/12}$	1.5	6.5	1067	< 20	2.2	12	51	99
UiO-66|$_{8.2/12}$	0.75	5	1400	92(7)	2.1	20	116	92
UiO-66-$(OH)_2$|$_{11/12}$	3.25	2	396	< 20	3.7	8	181	149
UiO-66-$(OH)_2$|$_{8.2/12}$	2	0	550	50(10)	3.2	6.5	128	142

Particle size has been calculated from TEM

Data not corresponding to this work have been obtained for references [39, 43-44].

Table 4. Adsorption capacity values for MOF-type UiO-66 and derivatives corresponding to different adsorbates

Adsorbate	adsorption capacity (mg/g)	MOF	reference
SCP**, 5 mg/L	50	UiO-66	[45]
SCP**, 25 mg/L	221	UiO-66	
SCP**, 45 mg/L	408	UiO-66	
SCP**	403	UiO-66, 273 K	
SCP**	339	UiO-66, 283 K	
SCP**	312	UiO-66, 293 K	
methylene blue	165.9	UiO-66-COOH-1	[46]
methylene blue	197.7	UiO-66-COOH-2	
methylene blue	157.5	UiO-66-COOH-3	
congo red	476.4	UiO-66-COOH-1	
congo red	401.1	UiO-66-COOH-2	
congo red	395.9	UiO-66-COOH-3	
ibuprofen	127.1	UiO-66	[47]
ibuprofen	50.69	UiO-66-NH_2	
naproxen	88.51.	UiO-66	
naproxen	40.10	UiO-66-NH_2	
methyl orange	84.8	UiO-66	[48]
congo red	13.2	UiO-66	
methylene blue	70.4	UiO-66	

rhodamine	67.5	UiO-66	
rhodamine, 273K	53.307	UiO-66	[49]
rhodamine, 303K	70.679	UiO-66	

*adsorption capacity in mg of adsorbate per g of UiO-66 or derivative MOF
**SCP is sulfachloropyridazine